INTERNATIONAL JOURNAL FOR NUMERICAL METHODS IN FLUIDS
Int. J. Numer. Meth. Fluids 2008; **58**:803–825
Published online 18 March 2008 in Wiley InterScience (www.interscience.wiley.com). DOI: 10.1002/fld.1768

Multiphase non-Newtonian effects on pulsatile hemodynamics in a coronary artery

Yong Hyun Kim[1], Pamela J. VandeVord[2] and Joon Sang Lee[1,*,†]

[1]*Department of Mechanical Engineering, Wayne State University, Detroit, MI, U.S.A.*
[2]*Department of Biomedical Engineering, Wayne State University, Detroit, MI, U.S.A.*

SUMMARY

Hemodynamic stresses are involved in the development and progression of vascular diseases. This study investigates the influence of mechanical factors on the hemodynamics of the curved coronary artery in an attempt to identify critical factors of non-Newtonian models. Multiphase non-Newtonian fluid simulations of pulsatile flow were performed and compared with the standard Newtonian fluid models. Different inlet hematocrit levels were used with the simulations to analyze the relationship that hematocrit levels have with red blood cell (RBC) viscosity, shear stress, velocity, and secondary flow. Our results demonstrated that high hematocrit levels induce secondary flow on the inside curvature of the vessel. In addition, RBC viscosity and wall shear stress (WSS) vary as a function of hematocrit level. Low WSS was found to be associated with areas of high hematocrit. These results describe how RBCs interact with the curvature of artery walls. It is concluded that although all models have a good approximation in blood behavior, the multiphase non-Newtonian viscosity model is optimal to demonstrate effects of changes in hematocrit. They provide a better stimulation of realistic blood flow analysis. Copyright © 2008 John Wiley & Sons, Ltd.

Received 28 September 2007; Revised 20 December 2007; Accepted 1 January 2008

KEY WORDS: coronary artery; computational method; RBC accumulation; non-Newtonian flow; hemodynamics; rheology

*Correspondence to: Joon Sang Lee, Department of Mechanical Engineering, Wayne State University, 5050 Anthony Wayne Dr. #2100 Detroit, MI 48202, U.S.A.
†E-mail: joonlee@wayne.edu

Contract/grant sponsor: Wayne State University Institute for Manufacturing Research (IMR); contract/grant number: 3-36037
Contract/grant sponsor: Wayne State University Office of the Vice President for Research; contract/grant number: 1-76068

INTRODUCTION

Hemodynamic stresses constitute one of the backbones of the development and progression of aneurysm or atherosclerosis. A reliable depiction of spatial distribution of shear stress in an artery provides a useful tool for studying the role of hemodynamic stresses in vascular diseases [1, 2]. The collection of red blood cells (RBCs) in specific areas of the arteries, such as in curved or bifurcated branches, is known to promote the development of atherosclerosis [3]. Thus, the optimization of computational models to better depict the fluid mechanics within the vessels is critical for designing clinical tools for diagnostic use.

Blood flow simulation is difficult to explain and predict since blood is a non-Newtonian fluid. Although a large number of investigations have led to a better understanding of the flow disturbances induced by an aneurysm or atherosclerosis, most theoretical and experimental studies have been performed under simplified assumptions. In several reports on arterial flow, blood is modeled as a Newtonian fluid [4–6]. The viscoelasticity of blood is ignored because shear rates in arteries whose diameters are larger than 0.5 mm [7] are predominantly high. Thus, the viscosity of blood is equal to the high shear rate limit viscosity of blood ($\eta_\infty = 3.5 \times 10^{-3}$ Pa s). Although non-Newtonian behavior is thought to have only a minor effect on flow characteristics in large diameter arteries, numerical simulations with a non-Newtonian fluid must be considered since blood has many components (RBCs, white blood cells (WBCs), platelets, and proteins). RBCs constitute the major cellular component of blood and are thought to determine its rheological behavior. Both shear thinning and viscoelasticity have been associated with RBC aggregation, deformation, and alignment [3].

Several properties of blood appear to play an important role in determining its behavior, such as shear rates and hematocrit levels. In the body, it is well known that blood behaves as a non-Newtonian fluid, particularly at low shear rates (less than around $100\,s^{-1}$) [8]. However, at high shear rate (over $100\,s^{-1}$), models tend to consider blood as a Newtonian fluid [8, 9]. Instantaneous cardiac cycle changes cause shear rate to vary from 0 to $1000\,s^{-1}$ in large vessels [10]. Hematocrit is the volumetric fraction of the RBCs in the plasma suspension. The range of hematocrit differs with gender and age. A female has a hematocrit range of 37–45%, and a male has 45–52% hematocrit [11]. The size of the vessel can influence hematocrit as well, with small vessel diameters (0.05 mm) reporting a low hematocrit of only 28% hematocrit [12].

One aspect of this study involves comparing the effects that non-Newtonian models have on the behavior of RBCs in blood. Blood is often modeled as a suspension of different particles but behaves more like an emulsion in fast flow. The suspending fluid in blood is plasma and it is composed of water and dissolved components (e.g. nutrients, protein, hormones, and waste products). Previous reports have treated plasma as a Newtonian, incompressible fluid [13, 14]. In this study, we will also assume plasma to be a homogeneous fluid.

Wall shear stress (WSS) is used as a key factor in characterizing arterial diseases [5, 15–17]. When non-Newtonian models of single-phase or multiphase flows are used, low WSS is observed on the inside curvature of realistic models [4, 18–20]. In addition, RBC accumulation in diseased vessels has been reported at the curvature [20, 21]. In atherosclerosis, the area of RBC accumulation and local flow characteristics (e.g. velocity, shear rate, and viscosity) are altered. RBC viscosity is high where RBC's accumulation is concentrated. The highest WSS magnitude is observed to be in regions with less accumulation and is higher than in the single-phase flow model [20].

Researchers have begun the development of experiments for multiphase blood flow models [22, 23]. Most non-Newtonian models are created using experimental data. Unfortunately, the

DOI: 10.1002/fld

information on cell transport, local concentration, or cell deposition is lacking in these models. Thus, further studies are needed to quantify the effects of flow characteristics and to determine the relationship of RBC accumulations with non-Newtonian models.

Secondary flow is another important aspect when simulating blood flow and its impact on RBC accumulation. In a curved artery, secondary flow plays a significant role in RBC accumulation and WSS which is known to be influenced by boundary layer thickness and migration of particle settling [3, 24–26].

In this study, we tested four different non-Newtonian viscosity models using the idealized coronary artery model. The purpose was to determine the appropriate methodology for identifying the effects of RBC accumulation and WSS. A comparison of different numerical models is done, and the effect of RBC on blood rheology is explained. For the first time, multiphase non-Newtonian models were used to investigate the relationship between the RBC volume fraction and the viscosity, shear rate, helicity, vorticity, and WSS. We expect that the results can ultimately be used to help predict the combination of these properties in human disease.

METHODS

Multiphase hemodynamic equations

Multiphase non-Newtonian models for hemodynamics are based on the Navier–Stokes equations and use the principle of mass, momentum, and energy conservation for each phase. The principal differences between the various non-Newtonian and single-phase models lie in the hematocrit of each model and in the relationship between shear rate and viscosity changes. In this study, four different non-Newtonian models are used: Carreau-Yasuda [20], Quemada [27], Cross [22], and Casson [28]. These models describe the shear-thinning rheological behavior of blood flow.

The continuity equation for each phase is given by

$$\frac{\partial(\rho_k \varepsilon_k)}{\partial t} + \nabla \cdot (\rho_k \varepsilon_k \mathbf{v}_k) = 0 \tag{1}$$

where ρ is the density, t is the time, ε_k is the volume fraction of each phase, and $\mathbf{v}$ is the velocity.

The sum of volume fraction of each phase must be equal to one

$$\sum_{k=1}^{n} \varepsilon_k = 1 \tag{2}$$

where k is the index of each phase and n is the total number of phases.

The momentum equation for each phase is given by

$$\frac{\partial}{\partial t}(\varepsilon_k \rho_k \mathbf{v}_k) + \nabla \cdot (\varepsilon_k \rho_k \mathbf{v}_k \mathbf{v}_k) = -\varepsilon_k \nabla p_k + \nabla \cdot \bar{\bar{\tau}}_k + \varepsilon_k \rho_k \mathbf{g}_k + \sum_{p=1}^{n} \mathbf{R}_{kp}(\mathbf{v}_k - \mathbf{v}_p) + \mathbf{F} \tag{3}$$

On the right-hand side of Equation (3), p is the pressure shared by all phases, $\bar{\bar{\tau}}$ is the shear stress, $\mathbf{g}$ is the gravity, $\mathbf{R}_{kp}$ is the interaction force coefficient between phases, $\mathbf{v}_k$ is the velocity of each phase, and $\mathbf{F}$ are the force terms, which are external force, lift force, virtual mass, and drag force between phases.

DOI: 10.1002/fld

The shear stress tensor $\bar{\bar{\tau}}_k$ is given by [29]

$$\bar{\bar{\tau}}_k = 2\mu_k \bar{\bar{D}}_k - \tfrac{2}{3}\mu_k \operatorname{tr}(\bar{\bar{D}}_k) \tag{4}$$

The deformation tensor $\bar{\bar{D}}_k$ is given by

$$\bar{\bar{D}}_k = \tfrac{1}{2}[\nabla \mathbf{v}_k + (\nabla \mathbf{v}_k)^{\mathrm{T}}] \tag{5}$$

Since blood is not a single-phase flow, the density of blood can be determined by

$$\rho_m = \varepsilon_r \rho_r + \varepsilon_p \rho_p \tag{6}$$

where r and p are the indexes for RBCs and plasma. The mixture density of blood is $1080\,\mathrm{kg/m^3}$, and the plasma density is $1000\,\mathrm{kg/m^3}$ [30].

Blood mixture viscosity is composed of RBC and plasma viscosities. WBC and platelet volume fraction are negligible and will not be considered. The mixture viscosity is given by

$$\eta = \varepsilon_r \mu_r + \varepsilon_p \mu_p \tag{7}$$

where μ_r and μ_p are RBC and plasma viscosities, and ε_r and ε_p are volume fractions of RBC and plasma.

Viscosity is a key factor in hemodynamic flow. Viscosity depends on hematocrit, shear rate, and temperature [12, 23, 31, 32]. In this study, temperature is assumed to be constant so that the effect of temperature on viscosity was not considered. The mixture viscosities η are summarized in Table I.

Table I. The viscosity models of mixture blood flow, η, given in cP as a function of strain rate, $\dot{\gamma}$, given in $\mathrm{s^{-1}}$.

Blood model	Mixture viscosity, η
Carreau-Yasuda model [20]	$\eta = \mu_p m[1+(\lambda\dot{\gamma})^2]^{n-1/2}$
	$m = 122.28\varepsilon_r^3 - 51.213\varepsilon_r^2 + 16.305\varepsilon_r + 1$
	$n = 0.8092\varepsilon_r^3 - 0.8246\varepsilon_r^2 - 0.3503\varepsilon_r + 1$
	$\lambda = 0.11\,\mathrm{s}, \mu_p = 0.001$
Quemada model [27]	$\eta = \dfrac{\mu_p}{\left[1-\frac{1}{2}\left(\frac{k_0+k_\infty\dot{\gamma}_r^{1/2}}{1+\dot{\gamma}_r^{1/2}}\right)\varepsilon_r\right]^2}$
	$\dot{\gamma}_c = 2.07, k_0 = 4.33, k_\infty = 1.88, \mu_p = 0.001, \dot{\gamma}_r = \frac{\dot{\gamma}}{\dot{\gamma}_c}$
Cross model [22]	$\eta = \mu_\infty + \dfrac{\mu_0 - \mu_\infty}{\left[1+\left(\frac{\dot{\gamma}}{\dot{\gamma}_c}\right)^P\right]}$
	$\mu_0 = 0.0364, \mu_\infty = 0.0035, \dot{\gamma}_c = 2.63\,\mathrm{s^{-1}}, P = 1.45$
Modified Casson model [28]	$\eta = \left(\sqrt{\mu_p} + \dfrac{\sqrt{\tau_0}}{\sqrt{\dot{\gamma}}+\sqrt{\dot{\gamma}}}\right)^2$
	$\mu_p = 0.001, \tau_0 = 0.021, \lambda = 11.5$

DOI: 10.1002/fld

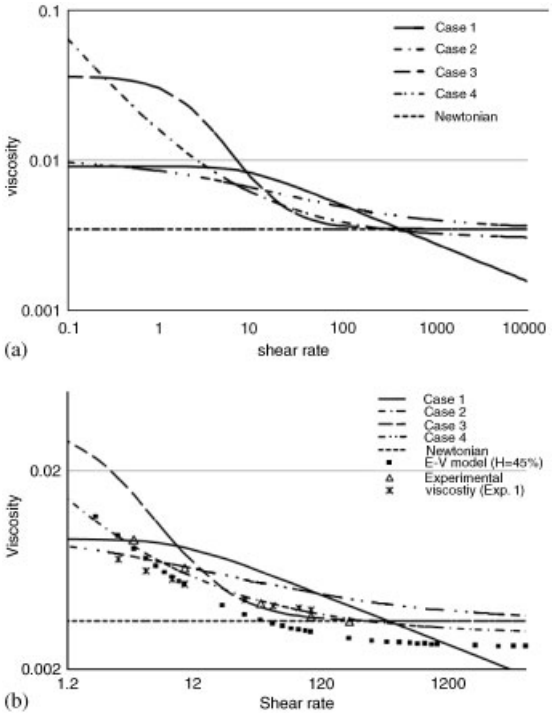

Figure 1. Viscosity with different non-Newtonian models (a) and with experimental data (b).

The Carreau-Yasuda, Quemada, Cross, and Casson models are commonly used non-Newtonian models [20, 22, 27, 28]. Figure 1 shows the blood viscosity profile as a function of strain rates for each non-Newtonian model. In multiphase flow, there is resistance to the motion caused by the interphase drag. The interphase momentum exchange coefficient, β_{kl}, between plasma and RBCs is determined by the Schiller and Naumann model [33, 34] as

$$\beta_{kl} = \frac{3}{4} C_{\mathrm{d}} \frac{\rho_p \varepsilon_p \varepsilon_r |\mathbf{v}_p - \mathbf{v}_r|}{d_r \phi} \tag{8}$$

where

$$C_{\mathrm{d}} = \frac{24}{Re_p}[1 + 0.15 Re_p^{0.687}] \quad \text{for } Re < 1000 \tag{9}$$

$$C_{\mathrm{d}} = 0.44 \quad \text{for } Re \geqslant 1000 \tag{10}$$

$$Re_p = \frac{\rho_p d_r |\mathbf{v}_p - \mathbf{v}_r| \phi}{\mu_p} \tag{11}$$

where d_r is the diameter of RBCs, ϕ is the shape factor, and C_{d} is the drag force on a single sphere. The interphase momentum exchange coefficient is related to the Reynolds number, Re_p. Other forces on each phase to be considered are the virtual mass and shear lift forces.

DOI: 10.1002/fld

The virtual mass force in the FLUENT code [33] is given by

$$\mathbf{F}_{\mathrm{vm},k} = 0.5\varepsilon_m \rho_k \left(\frac{\mathrm{d}_k \mathbf{v}_k}{\mathrm{d}t} - \frac{\mathrm{d}_m \mathbf{v}_m}{\mathrm{d}t} \right)\Bigg|_{k \neq m} \quad (\mathbf{F}_{\mathrm{vm},k} = -\mathbf{F}_{\mathrm{vm},m}) \tag{12}$$

where

$$\frac{\mathrm{d}\mathbf{v}}{\mathrm{d}t} = \frac{\partial \mathbf{v}}{\partial t} + (\mathbf{v} \cdot \nabla)\mathbf{v} \tag{13}$$

The shear lift force in the FLUENT code is given by

$$\mathbf{F}_{\mathrm{lift},k} = -0.5\varepsilon_m \rho_k (\mathbf{v}_k - \mathbf{v}_m) \times (\nabla \times \mathbf{v}_k)|_{k \neq m} \quad (\mathbf{F}_{\mathrm{lift},k} = -\mathbf{F}_{\mathrm{lift},m}) \tag{14}$$

The virtual mass effect occurs when one phase accelerates relative to the other phase. The lift force acts on a particulate phase due to velocity gradients in the primary phase flow field [20]. For our study, only the virtual mass force was included.

NUMERICAL METHODS

In this study, we used the multiphase three-dimensional Eulerian–Eulerian method in FLUENT [33]. The numerical solution method consists of a finite volume, unstructured mesh, and staggered grid arrangement. The momentum equations were solved with a staggered mesh, whereas the continuity equations were solved using a donor cell method. The two-phase Eulerian–Eulerian method was used and validated using Ding *et al*. [35] and Jung *et al*. [20]. The non-Newtonian viscosity models given in Table I and the pulsatile inlet velocity for the cardiac cycle were programmed into the FLUENT code as a user-defined function.

All simulations of the idealized rigid curved coronary artery model were carried out using the three-dimensional computational domain (Figure 2). Further simplification in our study concerned the numerical model. The momentum and mass conservation equations have to be solved under difficult boundary conditions in order to fully model the blood flow in arteries. All physiological parameters have to be accounted for, i.e. wall compliance, pulsatile flow, and non-Newtonian behavior of the blood. In addition, in a coronary artery, cardiac contraction induces a continuous, site-specific motion, and deformation of the vessel. All these aspects may affect flow patterns and were thoroughly studied in the past years [36–38]. The impact of the assumption of rigid or non-rigid arterial walls has been well investigated in the literature [37, 38]. However, Ernst *et al*. [39] agree that the assumption of a rigid wall is sufficiently accurate for WSS profiling in investigating atherosclerosis for clinical purposes. Among the deformation of the coronary arteries due to cardiac surface motion, only torsion is assumed to have a limited effect on local WSS [39]. Also the appropriate compliance value to apply to coronary arteries tethered to or embedded in the pericardium is unclear and the importance of coronary artery compliance on the flow field is difficult to estimate [37].

The artery diameter, D, was 4.37 mm, the radius of curvature, R, was 4.15 cm, and the ratio of the diameter of the artery and curvature, (R/a), was 19. This ensured a fully developed inlet velocity profile. A mesh was generated by GAMBIT [34] with the Cooper mesh generation algorithm. The total number of nodes for the mesh was 57 960. A mesh refinement test has been conducted with twice and fourth times the number of computational cells. Comparisons between the baseline and

DOI: 10.1002/fld

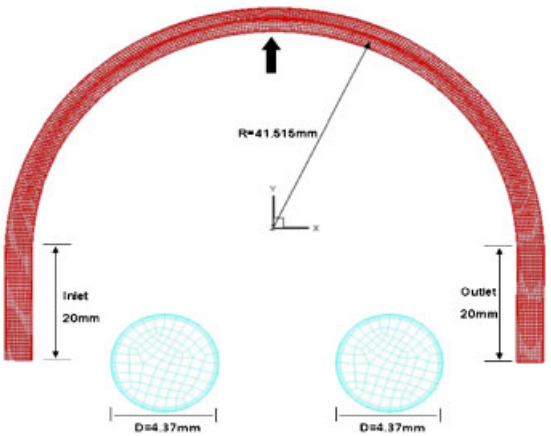

Figure 2. Three-dimensional computational grid of an idealized curvature coronary artery.

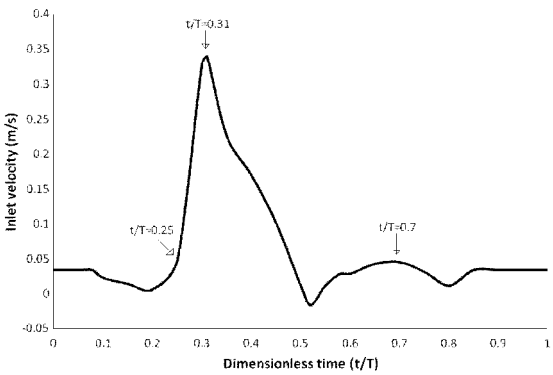

Figure 3. Inlet pulsatile coronary velocity for RBCs and plasma. End diastole ($t/T=0.25$), peak systole ($t/T=0.31$), and beginning of diastole ($t/T=0.70$).

the finer grid systems show a maximum difference of 3.4% for the velocity across the artery at the center line.

A pulsatile inlet velocity profile was used for RBCs and plasma and the outlet constant pressure was adapted following Jung *et al.* [20]. The maximum velocity magnitude was 0.35 m/s at $t'(=t/T)=0.31$ and minimum was -0.01 m/s at $t'=0.52$, where t', t, and T were dimensionless time step, computation time step, and total time step, respectively. Most results were obtained at three different points in the pulsatile velocity (Figure 3): the end diastole ($t/T=0.25$), peak systole ($t/T=0.31$), and beginning of diastole ($t/T=0.7$). These points have been previously found to be significant [30]. RBCs and plasma employed the zero slip boundary conditions on the wall. The inlet and initial volume fractions of RBCs were maintained constant at five different hematocrit percentages, 37, 40, 45, 50, and 52% (Table II). These hematocrit percentages were selected in female and male hematocrit ranges. The initial velocities of RBCs and plasma were set to zero.

DOI: 10.1002/fld

Table II. Cases of four non-Newtonian models with five different hematocrits.

Inlet hematocrit (%)	Carreau-Yasuda	Quemada	Cross	Casson
37	Case 1-1	Case 2-1	Case 3-1	Case 4-1
40	Case 1-2	Case 2-2	Case 3-2	Case 4-2
45	Case 1-3	Case 2-3	Case 3-3	Case 4-3
50	Case 1-4	Case 2-4	Case 3-4	Case 4-4
52	Case 1-5	Case 2-5	Case 3-5	Case 4-5

The exit constant pressure was 10200 Pa s above gauge pressure. All computations were completed in three cardiac cycles.

We considered RBCs as spherical particles with an average diameter of 8 μm and a shape factor, $\phi = 1$. The mean inlet Reynolds number was 195, based on average inlet velocity. The Womersley number was 3.21. The Dean number, $Dn = Re/\sqrt{(R/a)}$, characterizing curved tube flow, was 53. We performed simulations based on changes in RBC accumulation, viscosity, velocity, shear rate, secondary flow, and WSS with each of the four different viscosity models during the proposed cardiac cycles.

RESULTS

The presentation of results focuses on non-Newtonian multiphase flow on the curved coronary artery. Published reports on the velocity distribution for unsteady, single-phase, non-Newtonian, and Newtonian fluids [30, 40], and the multiphase non-Newtonian flow with the Carreau-Yasuda model were compared with a single-phase non-Newtonian model with the curved coronary model [20].

Viscosity changes with respect to different hematocrits. With low hematocrit, the maximum blood viscosity decreases and shifts down, making the non-Newtonian fluid viscosity smaller than in the Newtonian fluid for the shear rate ranging from 10 to 100 s^{-1}. As shown in the Carreau-Yasuda model, parameters are a function of shear rate and hematocrit. Parameters of the Carreau-Yasuda model of 45% hematocrit case are in good agreement with Wojnarowski's rheological data [20, 31]. The Quemada model is also known to match with the combination of the empiric and the Vand models [23, 27] and the experimental data [41] as shown in Figure 1(b). The Cross model [22] shows high viscosity at lower shear rates. The range of viscosity is observed to be larger in the Cross model when compared with those of other models. The Cross and Casson models show the same trend as the experimental data.

Non-Newtonian models with 45% hematocrit

The two-phase flow model of RBCs and plasma was initially simulated with 45% inlet hematocrit. Figures 4(a)–(c) show the axial velocity profiles at the B–B' cross section at $t/T = 0.25$, 0.31, and 0.70, which are the end diastole, peak systole, and beginning diastole, respectively. At each time step, the velocity profiles of the four non-Newtonian models were compared. In Figure 4(d), the axial velocities of five different planes were plotted at the A–A' cross section at different time steps.

DOI: 10.1002/fld

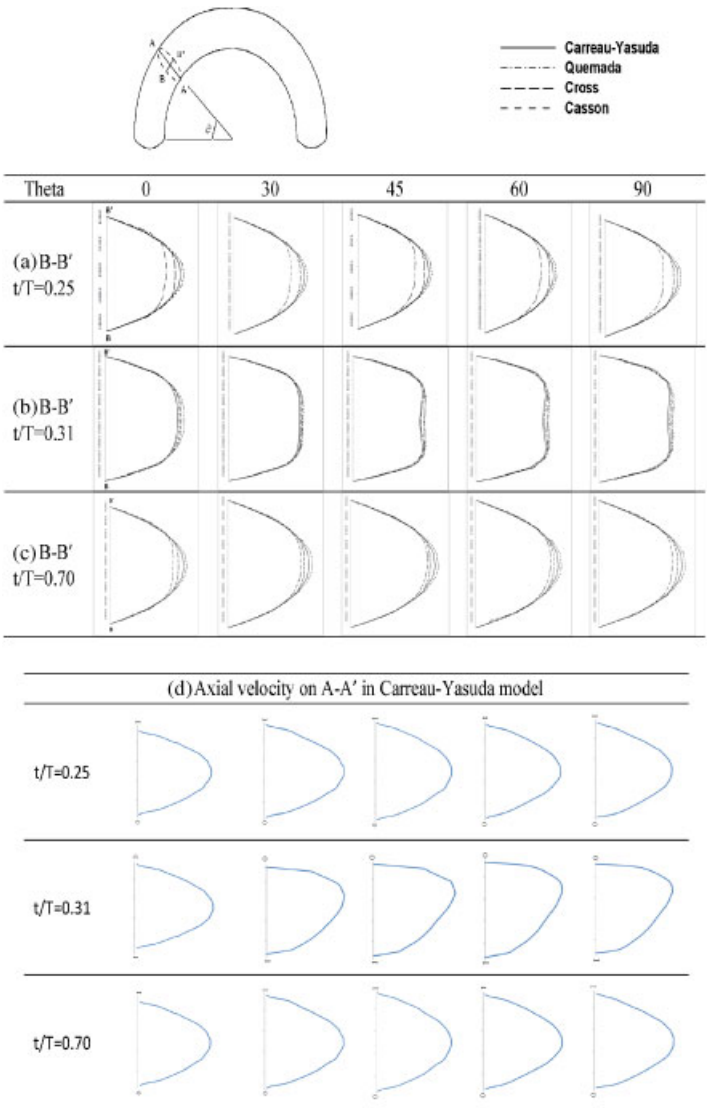

Figure 4. The axial velocity in B–B' with 45% inlet hematocrit at (a) $t/T=0.25$ (end diastole), (b) $t/T=0.31$ (peak systole), and (c) $t/T=0.70$ (beginning of diastole). The axial velocity vector and contour plot on A–A' in Carreau-Yasuda model (d). At the peak systole, the flatted velocity profiles were showed on B–B' and the highly skewed outside the curvature on A–A'. At the slow velocity ($t/T=0.25$ and 0.70), velocity profiles were symmetric.

Influence of the cardiac cycle. At end diastole ($t/T=0.25$) and the entrance of the curved artery ($\theta=0$), the axial velocity is flattened as shown in Figure 4(a). At A–A' in Figure 4(d), the axial velocity of the Carreau-Yasuda model (Case 1-3) shows a distribution to be slightly skewed towards the outside curvature. Quemada model (Case 2-3) has a more flattened velocity profile than other

DOI: 10.1002/fld

models. Casson model (Case 4-3) shows that its velocity profiles are similar to a fully developed Newtonian fluid. At this time step, the inlet velocity magnitude is very small (0.009 m/s) and the secondary flow is barely observed (B–B') due to the low inlet velocity magnitude.

At peak systole, the inertia forces (taking account of the acceleration of the fluid) dominate the flow features. The axial velocity increases but is not dominated by the secondary flow, resulting in blunter axial velocity distributions. The viscous layer along the inner wall is thinner and the velocity gradient is observed to be larger. The maximum velocity shifts towards the outside wall from a 45° plane in the curvature. The shear stress on the outside curvature also increases and is greater than on the inside curvature. RBC viscosity plots show profiles to be similar to the velocity profile. From a 45° plane, the secondary flows increase and are stronger. The secondary flows at the B–B' cross sections are characterized by two vortices with weak flow in the center and stronger flow in the boundary layer, which is confirmed by previous research [20]. The secondary flow shows essentially the same features during the beginning and end of the systole (before and after peak systole). In Figure 4(b), the axial velocity of Case 2-3 is fast at the center of the curvature, and thus the secondary flow is observed to be weaker than in other cases. The secondary flow of Case 4-3 is the strongest due to a more blunted axial velocity.

After peak systole, the inlet velocity decreases and the velocity magnitude becomes small as in the end diastole (Figure 4(a)). Secondary flow does not significantly affect the axial velocity at this time step (Figure 4(c)) and the shift of the axial velocity towards the outer wall in the plane is not pronounced (Figure 4(d)). Case 2-3 have the lowest axial velocity and Case 4-3 has the fastest axial velocity at the center of the curvature.

In the 45% inlet hematocrit case, all four different viscosity models demonstrate high RBC accumulation on the inside curvature (Figure 5). This flow characteristic is observed in Jung *et al*. [20]. Small velocity magnitude has high RBC accumulation and large velocity has low RBC accumulation (Figure 4). In Figures 5(a) and (c), Case 2-3 has more RBC accumulation on the inside curvature compared with other models due to the slow axial velocity and high secondary flow. The least RBC accumulation is shown in Case 4-3 due to the fast axial velocity and low secondary flow (Figures 4(a) and (c)). Figure 6 demonstrates that Case 2-3 has a fast axial velocity and small RBC accumulation on the inside curvature, but Case 4-3 has low axial velocity and large RBC accumulation (Figure 4(b)).

Non-Newtonian models tested with various hematocrit levels

The computed maximum RBC volume fraction was determined to be found on the inside curvature of the artery with a 45% hematocrit level. This appears to be related to the secondary flow. However, RBC accumulation could be explained with other flow characteristics, such as viscosity, shear rate, and WSS. We examined each of these characteristics individually.

Viscosity effects. Local viscosity and velocity were observed to examine if a relationship occurs with local RBC volume fraction. Viscosity on the inside radius curvature was higher than the outside curvature (Figure 6) and velocity near the inside curvature is lower than near the outside curvature (Figure 7). With these results, local low velocity has local high viscosity, thus leading to a high RBC accumulation. Another explanation of RBC accumulation is that the effect of inlet hematocrit on the velocity is similar to that of viscosity in all cases. Figure 7 demonstrates that the center curvature at different constitutive equations predict distinctive velocity profiles. The axial velocity is compared with different non-Newtonian models at five different inlet hematocrit

DOI: 10.1002/fld

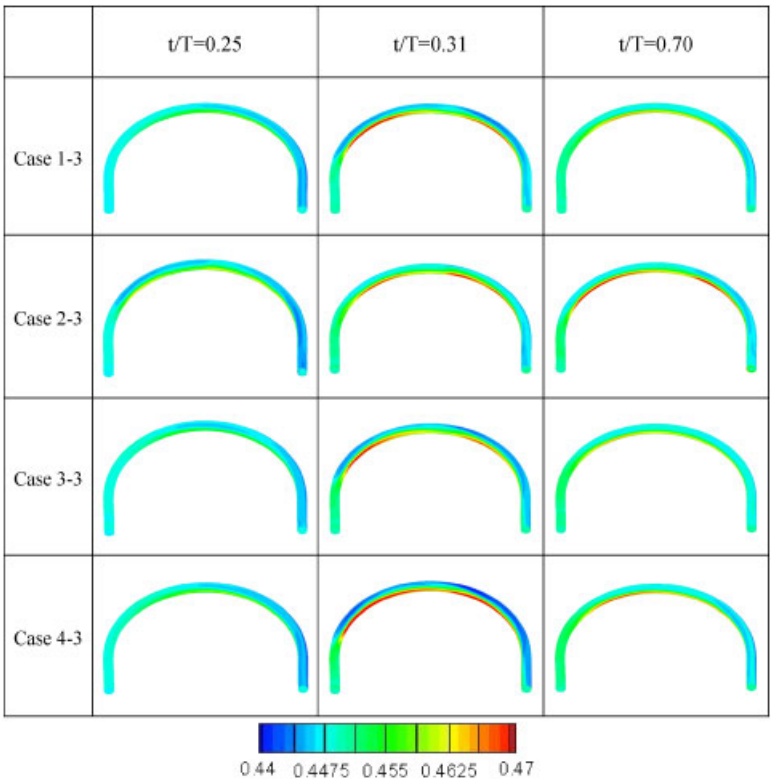

Figure 5. RBC volume fraction with 45% inlet hematocrit case at $t/T = 0.25$, 0.31, and 0.7. The RBC accumulations occurred inside the curvature where the flow velocity was slow. The outside curvature had low RBC accumulation due to the high velocity.

percents. For axial velocity profile, the maximum velocity exhibited a percentage variation of up to 2.6% in Case 1 and 4.5% in Case 2 in the center of the artery (Figure 7). With an increase in inlet hematocrit, the velocity magnitudes increase comparing Cases 1 and 2. The difference in the velocity profiles is pronounced at the center of the artery and the difference diminished away from the centerline in all hematocrit percents. However, in Cases 3 and 4, the differences in velocity profiles are very small. These velocity magnitudes decrease with an increase in inlet hematocrit. This is acceptable in light of the fact that the velocities of Cases 1 and 2 have the highest viscosity effect and the velocities of Cases 3 and 4 have the smallest effect with inlet hematocrit changes. Thus, high inlet hematocrit leads to high viscosity of blood and low inlet hematocrit leads to low viscosity (Figures 6 and 7). In Cases 3 and 4, the high effect of hematocrit appears to be located on the inside curvature (at radius $= -1$); thus these models may not be beneficial to use with all inlet hematocrits. One possible reason why the overall viscosity is getting lower with higher inlet hematocrit is because of fixed mixture blood viscosity value as described in Equation (7).

RBC viscosity is compared in different inlet hematocrits and different non-Newtonian models with velocity magnitude of Case 1 (Figure 8). Viscosity is shown to follow an inverse process due to shear-thinning behavior. All non-Newtonian models have a similar trend for viscosity change

DOI: 10.1002/fld

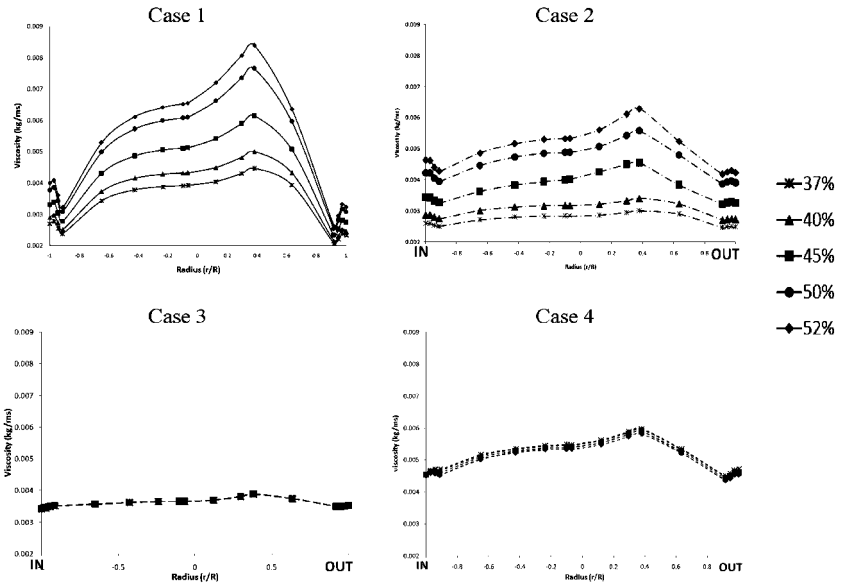

Figure 6. Viscosity change with hematocrit in four non-Newtonian viscosity models at peak systole. In Cases 1 and 2, the viscosity increased with increased inlet hematocrit, but the viscosities of Cases 3 and 4 did not change with increased inlet hematocrit. Viscosities on the inside of curvature (left side of the graph) were higher than on the outside curvature due to the velocity. The highest viscosity explained the RBC aggregation.

with different inlet hematocrits. The viscosities of Cases 1 and 2 on the inside curvature are larger than on the outside curvature and increase with a higher level of inlet hematocrit on both sides of the curvature. It should also be noted that the difference in the viscosity between the inside and outside curvature increases with higher levels of inlet hematocrit. However, in Cases 3 and 4, viscosities are lower on the inside curvature compared with those of the outside curvature. They decrease with the increase in the inlet hematocrit on both sides of the curvature, which is already observed in Figure 6. Overall, the maximum viscosity in all non-Newtonian models occurs at beginning diastole ($t/T=0.7$) and the minimum viscosity is observed at peak systole ($t/T=0.31$) in all hematocrit cases. The differences in viscosity between the inside and the outside curvatures are almost up to 40% at the peak systole. Also, a large difference between the inside and the outside curvatures is observed at end systole ($t/T=0.7$). The differences vary from 100 to 233% on the inside curvature and from 233 to 344% on the outside curvature at end systole. Therefore, in the same inlet hematocrit, the inside curvature has higher viscosity than the outside curvature during the cycle except when the velocity decreases and hits low values. The difference in the viscosity between the inside and outside curvatures increases with the increase of inlet hematocrit in Cases 1 and 2. The opposite occurs in Cases 3 and 4 as they decrease with higher inlet hematocrit during the cycle.

RBC volume fraction effects. In all cases examined, RBC volume fractions are associated with inlet velocity profiles on the inside curvature (Figure 9). Overall, the highest volume fractions are observed after peak systole. Cases 1 (Carreau-Yasuda model) and 2 (Quemada model) show the

DOI: 10.1002/fld

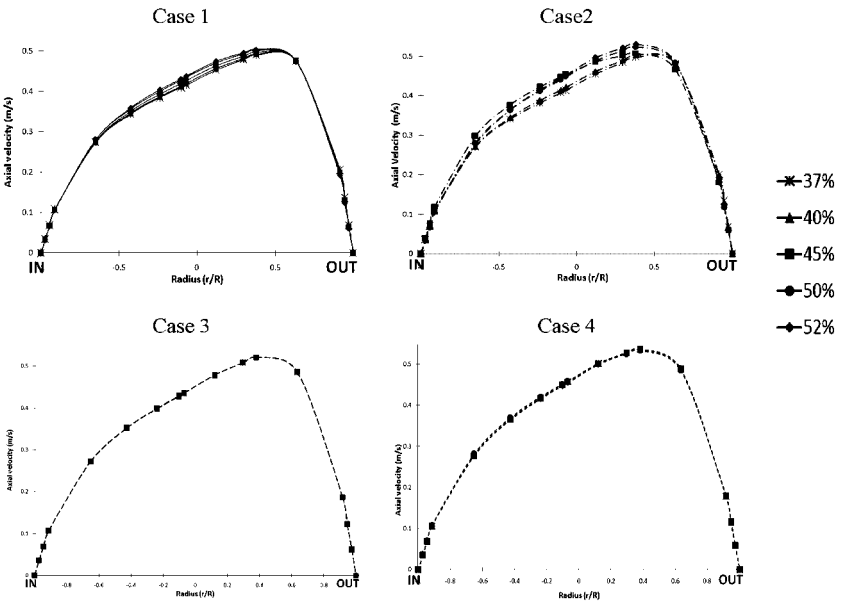

Figure 7. Velocity plots of different viscosity models with different hematocrits. In Cases 1 and 2, the velocity increased with increased inlet hematocrit but decreased in Cases 3 and 4. The point of high velocity magnitude was skewed outside regarding the geometry.

difference of RBC volume fraction between the inside and outside curvatures, which increases with high inlet hematocrit. In contrast, Cases 3 (Cross model) and 4 (Casson model) demonstrate that the differences of RBC volume fraction between both side curvatures decrease with high inlet hematocrit. In comparison, Cases 1 and 2 are more suitable to use with all inlet hematocrit variations and provide a better understanding of the relationship among inlet hematocrit, RBC accumulation, viscosity, velocity, and other flow characteristics (e.g. shear rate and WSS).

The RBC volume fraction and RBC density are related inversely as indicated in Figure 10 because of the fixed mixture density. It can be observed that the RBC volume fraction is sensitive to RBC density. The RBC volume fraction contour shows maximum values on the inside curvature which are similar to the lowest values of RBC density plots at peak systole in all non-Newtonian cases of 45% inlet hematocrit. This is explained from the density formulation (Equation (6)). Therefore, the maximum of RBC volume fraction is expected to occur at the lowest RBC density values.

The relationship among RBC volume fraction, viscosity, velocity, and WSS values are shown in Figure 11 with the different non-Newtonian models at 45% inlet hematocrit. Since Cases 3 and 4 were optimized under specific hematocrit assumption (Hct = 40–45%), these results were used in this study. It is observed that viscosity and RBC volume fraction decrease with the increase in the velocity profile. In addition, WSS increases with the increase in the velocity on the inside curvature around peak systole. This relationship is consistent in all models. On the outside curvature, Cases 1 and 2 show that the RBC volume fraction increases with the increase of velocity, whereas Cases 3 and 4 show that the RBC volume fraction decreases with the increase of velocity. However, WSS and viscosity follow the phenomenon observed on the inside curvature.

DOI: 10.1002/fld

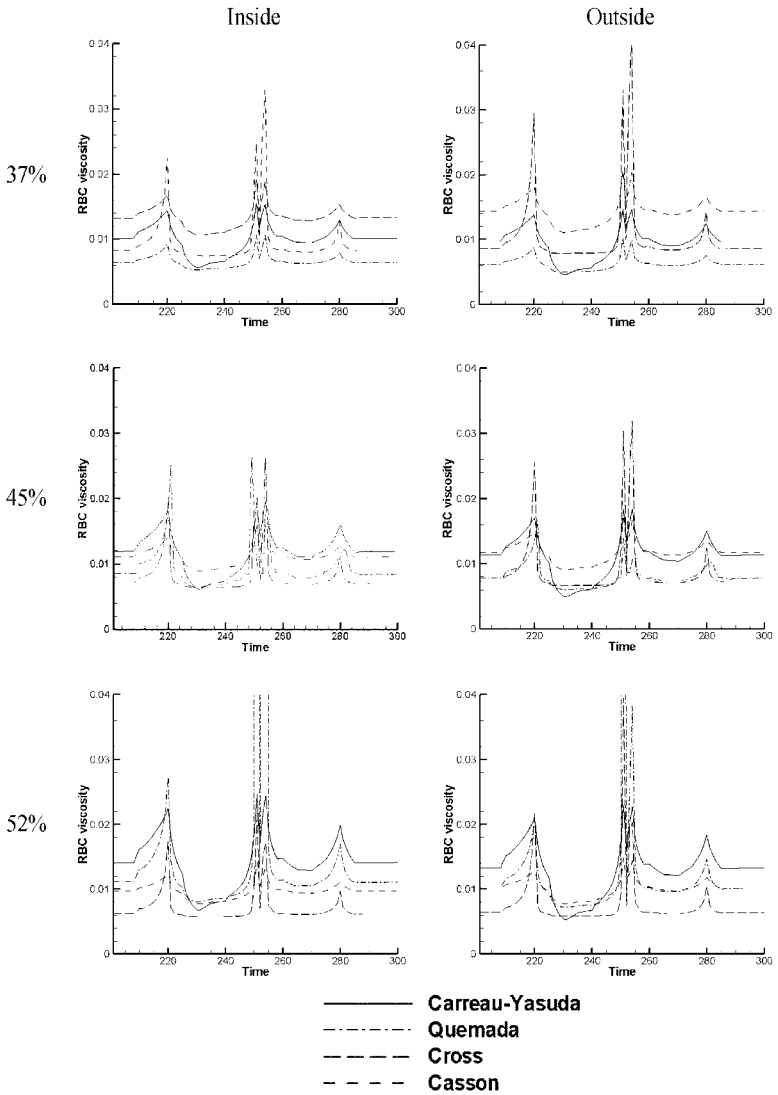

Figure 8. Viscosity changes with different hematocrit percents. The lowest viscosity occurred in the peak systole ($t/T = 0.31$) and the highest occurred in the deceleration systole ($t/T = 0.7$). Viscosities in Cases 1 and 2 increased with high hematocrit but in Cases 3 and 4 decreased during the cycle.

Shear rate and WSS effects. Since velocity and viscosity can be explained by RBC volume fraction, the higher-order flow characteristics (e.g. shear rate and WSS) should be analyzed with variations in RBC volume fraction, velocity, and viscosity. Shear rate and WSS for different non-Newtonian models follow inlet velocity profile for both inside and outside curvatures (Figure 12). Shear rate and WSS at the inside curvature are lower than at the outside curvature due to skewed axial velocity. Figure 12(b) depicts Case 4-3 (45% hematocrit case of the Casson model) as having a higher WSS compared with other non-Newtonian models, due to low RBC volume fraction on the

DOI: 10.1002/fld

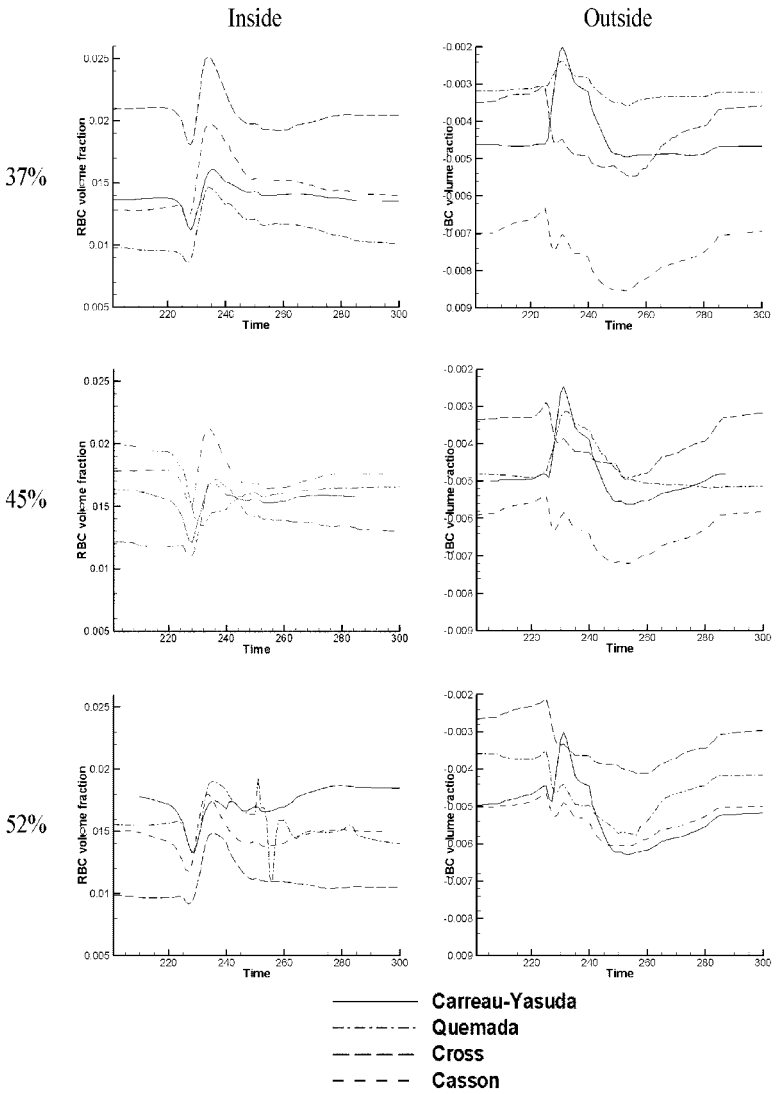

Figure 9. RBC volume fractions during the third cycle with different hematocrit percents. The volume fraction showed that the RBC accumulated inside of curvature in all cases. On the inside curvature, the low volume fraction differences occurred at the starting point of acceleration systole. On the outside curvature, the volume fraction differences were small on the peak systole ($t/T = 0.31$) in Cases 1 and 2, but in Cases 3 and 4, the volume fraction differences were small before acceleration systole ($t/T = 0.25$) and increased the differences.

inside curvature at peak systole. For shear rate, Case 4-3 is the lowest and Case 2-3 is the highest on the inside curvature (Figure 12(a)). On the outside curvature, Case 4-3 is the lowest and Case 1-3 is the highest (Figure 12(b)). WSS and viscosity in Case 4-3 are also observed to be higher than other 45% inlet hematocrit cases on both side curvatures (Figures 8 and 12(b)), RBC volume

DOI: 10.1002/fld

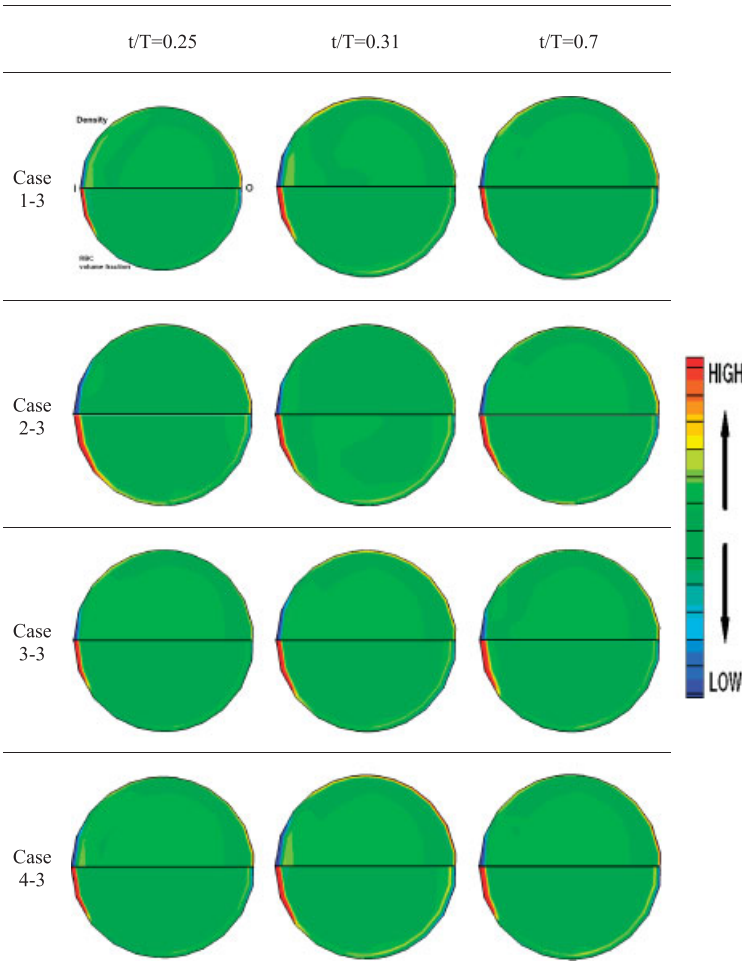

Figure 10. RBC density (upper hemi-circle) and RBC volume fraction (lower hemi-circle) are compared. RBC density was low at the region of high RBC volume fraction according to the multiphase flow equation.

fraction is the highest on the inside curvature and the lowest of other 45% inlet hematocrit cases on the outside curvature (Figures 9). Therefore, it can be stated that WSS is affected by viscosity and the RBC volume fraction on the inside curvature. However, viscosity has more of an effect on the WSS and RBC volume fraction on the outside curvature. It appears that shear rate does not affect WSS.

Helicity and vorticity effects. Helicity and vorticity contour plots were examined to determine the effect of inflow pulsatile conditions (Figure 13). The helicity is defined as

$$\varphi = (\nabla \times U) \cdot U \tag{15}$$

DOI: 10.1002/fld

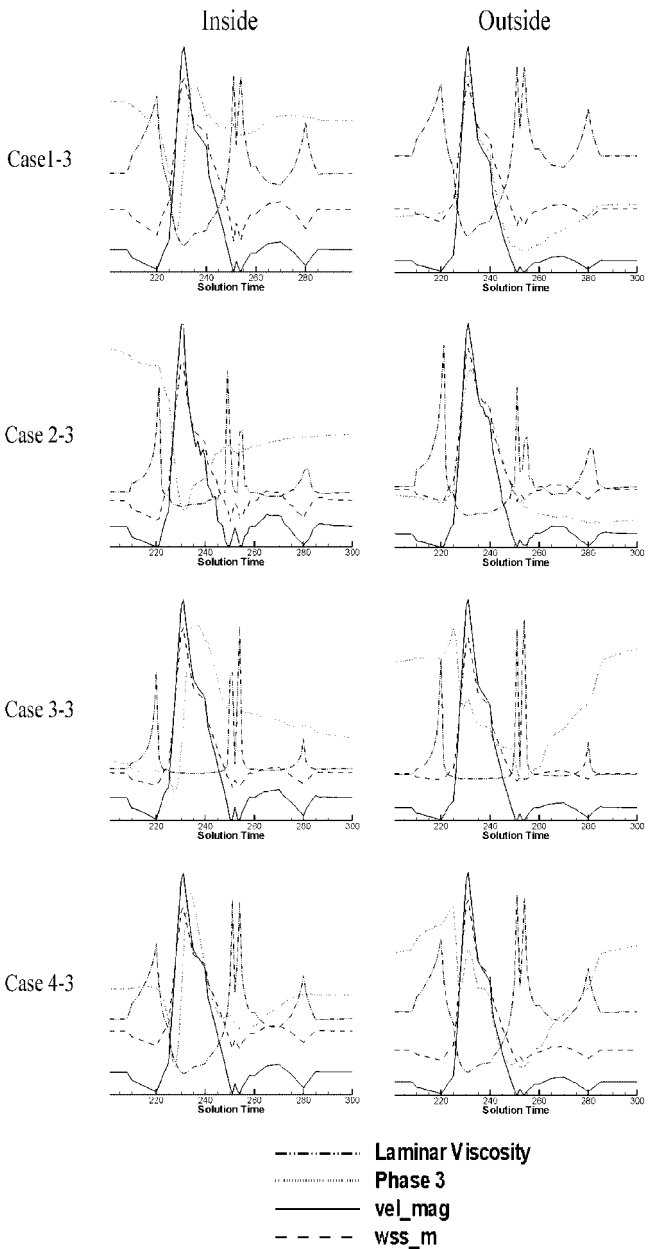

Figure 11. WSS, velocity magnitude, viscosity, and RBC volume fraction of all cases in 45% inlet hematocrit. The viscosity was related to the velocity inversely. The graphs of WSS and RBC volume fraction were same as of the velocity magnitude.

DOI: 10.1002/fld

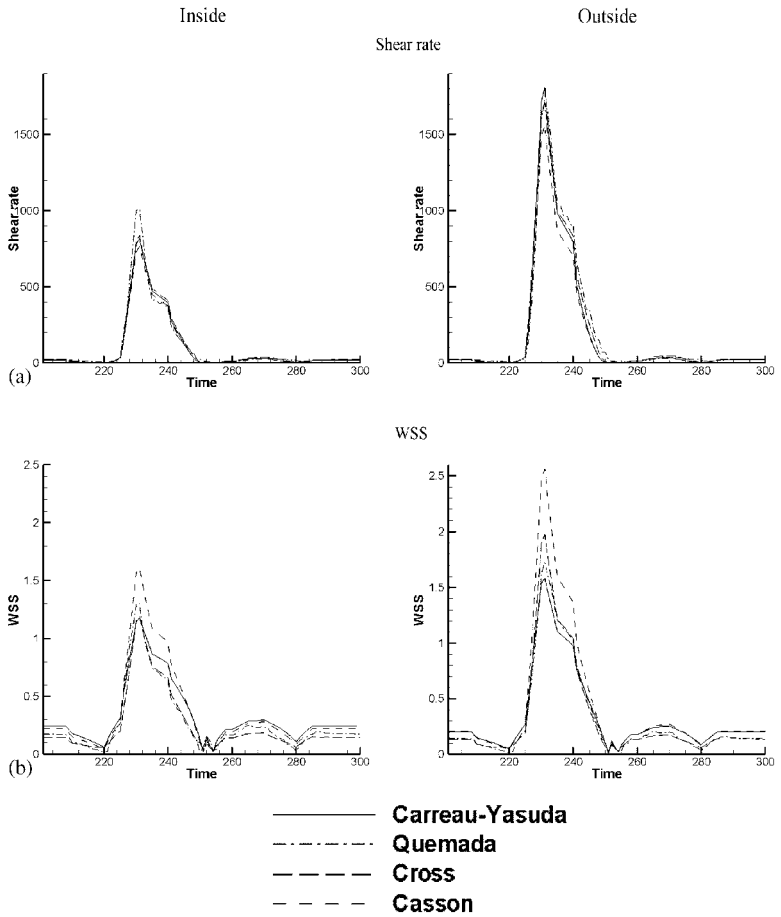

Figure 12. Shear rate (a) and WSS (b) of all cases in 45% inlet hematocrit. Shear rate and WSS showed that the outside curvature had higher magnitude than the inside curvature. The magnitude of WSS was decided by viscosity more than by shear rate at the peak systole.

This represents the transfer of vorticity to a fluid parcel in convection motion. If a parcel of fluid is undergoing solid body motion rotating about an axis parallel to the direction of motion, it will have helicity. Contour plots at the A–A' plane $\theta = 90°$ were created for each case. Figure 13 demonstrates that the helicity (φ) in each case is high near the boundary layer of the outside curvature. At peak systole ($t/T = 31$), the core helicity and vorticity shift towards the outside curvature as the velocity magnitude.

In Figure 13, secondary flows with contour plots are shown at the selected region, which is indicated in Figure 1. Secondary flow increases during the systole cycle; however, during the diastole cycle, it maintains the small flow magnitude. Its behavior can be analyzed with helicity, which is related to fluid motion and is affected by velocity and vorticity. The helicity is skewed towards the outside curvature as is the velocity profile. The core of helicity also moves towards the upside and downside boundary layers. High helicity magnitudes are shown at the boundary layer region where high vorticity exists. High vorticity and helicity regions on the outside curvature

DOI: 10.1002/fld

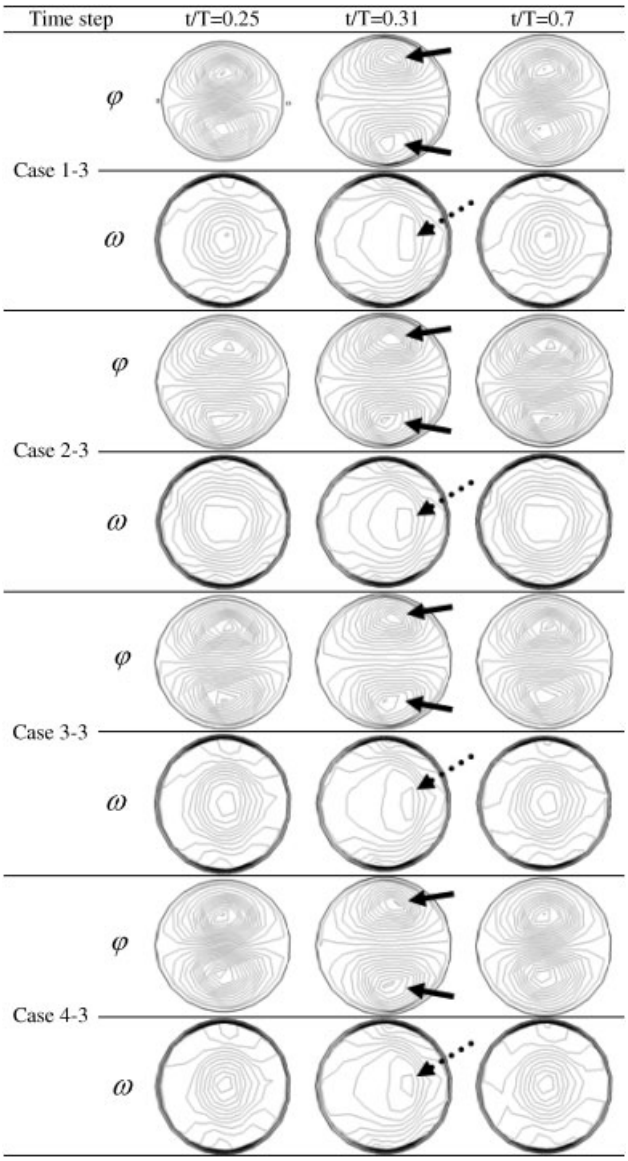

Figure 13. Helicity (φ) and vorticity (ω) in each viscosity model at the end diastole, peak systole, and beginning of diastole (Hct = 45%). At the peak systole, helicity (rigid arrow) moved the outside curvature and near the artery and the lowest of vorticity (dotted arrow) skewed outside curvature. The movement of vorticity and helicity made RBC accumulate on the inside curvature where it had the slow flow velocity.

have a smaller RBC volume fraction. On the inside curvature, the velocity and vorticity are very small, and the helicity effect is also insignificant. As a result, the RBC volume fraction is larger on the inside curvature than on the outside curvature.

DOI: 10.1002/fld

DISCUSSION AND CONCLUSION

This study demonstrates that RBCs accumulate on the inside curvature of the coronary artery model with multiphase flow simulation. The results are analyzed with four non-Newtonian models, which have not been previously accomplished with multiphase flow simulation. Multiphase non-Newtonian models are computed to predict the accumulation of RBC on the inside curvature of a coronary model. Several flow characteristics are varied to investigate the effects they have on RBC accumulations within the four non-Newtonian models. Each model has different flow characteristics with a function of shear rate, but all models show that shear rate and WSS are related to the inlet velocity profile. Carreau-Yasuda (Case 1) and Quemada (Case 2) models are the function of hematocrit and shear rate, but the other two models, Cross (Case 3) and Casson (Case 4), are the function of only shear rate. To our knowledge, this comparison of multiphase non-Newtonian models is the first made.

In general, Carreau-Yasuda, Quemada, Cross, and Casson models represent shear-thinning behavior, and at a specific shear rate, these models do coincide with each other. The Carreau-Yasuda model with a 45% hematocrit conformed well at low shear rate ranges, while at higher shear rate ranges the Casson and Quemada models with a 45% hematocrit converged with the Carreau-Yasuda model. The Cross model changed dramatically at low and high shear rate ranges and fitted at the middle shear rate ranges. The Casson model converged with the Carreu-Yasuda model at higher shear rate ranges. However, in this study, these non-Newtonian models may not be available to use for all the numerical blood flow simulations. With different inlet hematocrits, the Carreau-Yasuda and Quemada models were more suitable to use in multiphase flow compared with the Cross and Casson models that have a function of only shear rate. The Carreu-Yasuda model can be useful in all inlet hematocrit cases. However, we predict that the Quemada model should not be used in conditions of higher inlet hematocrit cases (Hct$>$50%) as it was shown to have an unstable RBC volume fraction (Figure 8) and viscosity (Figure 9). The Cross and Casson models showed that the change of RBC volume fraction and viscosity were related with inlet hematocrit but the flow characteristics with local hematocrit was not unacceptable to use in multiphase flow simulations.

The variability of rheological models can be reflected in velocity, secondary flow, RBC viscosity, RBC volume fraction, shear rate, WSS, vorticity, helicity, mass transfer, and pressure distribution. In this study, several variables were considered. Velocity, secondary flow, helicity, and vorticity influenced RBC accumulations on the inside curvature. WSS and shear rate on the inside and outside curvatures were observed to be similar to results from multiphase computational fluid dynamics model simulations [20]. The lower shear rate in the central region of the curved section produced a high viscosity because of the shear-thinning behavior in all non-Newtonian models. This effect caused the flow of RBCs to migrate preferentially through the boundary layer. Its behaviors were observed in all the different inlet hematocrit cases using the Carreu-Yasuda and Quemada models. RBCs concentrated on the inside curvature and RBC viscosity during diastole was higher than during systole because of a low shear rate. The WSS trend on the inside and outside curvatures could be explained with RBC volume fraction and viscosity. Shear stress was the second term on the right-hand side of momentum equations given by Equation (3). The biomechanical force on the inside curvature of the artery vessel, coupled with low oscillatory WSS, may damage the endothelium, thus ultimately leading to a progression in atherosclerosis development (adhesion of monocytes and platelets) as described by Stary [42].

DOI: 10.1002/fld

The non-Newtonian models with a function of hematocrit were observed to be more effective in velocity and viscosity profiles when the flow characteristics with different inlet hematocrit cases were analyzed. The non-Newtonian models, without the effect of hematocrit change, have almost the same velocities and viscosities in the center of the artery despite different inlet hematocrits. Only near the wall does viscosity make a difference. There was a significant difference in velocity and viscosity among inlet hematocrit percents in terms of effect on the models having a function of hematocrit. Higher hematocrit cases had denser flow and caused high viscosity and lower velocity near the wall. They produced higher maximum velocity at the center of the artery.

We determined that the non-Newtonian models with inlet hematocrit were more suitable to analyze the realistic hemodynamic behavior than without inlet hematocrit. Although experimental studies involving clinical data need to be conducted, our results established that variations of inlet hematocrit yield significant hemodynamic differences and should be considered to accurately depict disease formation in the curved coronary artery.

NOMENCLATURE

Hct	hematocrit
ρ	density, kg/m^3
η	mixture viscosity, Pa s
μ	viscosity of each phase, Pa s
μ_∞	infinite mixture viscosity, Pa s
μ_0	zero mixture viscosity, Pa s
$\mathbf{v}$	velocity, m/s
ε	volume fraction
$\bar{\bar{\tau}}$	shear stress tensor
$\bar{\bar{D}}$	deformation tensor
β_{kl}	interphase momentum exchange coefficient
ϕ	red blood cell (RBC) shape factor
C_d	drag coefficient on a single sphere
$\mathbf{F}$	force terms
$\mathbf{F}_\mathrm{vm}$	virtual mass force, N
$\mathbf{F}_\mathrm{lift}$	shear lift force, N
Re	Reynolds number
Dn	Dean number
R	radius of curvature, cm
a	artery radius, mm
D	artery diameter, mm
t'	dimensionless time, t/T
T	total computation time, s
θ	angle from a curvature entrance
$\dot{\gamma}$	shear rate, s^{-1}
$\dot{\gamma}_r$	relative shear rate, s^{-1}
$\dot{\gamma}_c$	defined by phenomenological kinetic model
λ	time constant at the Carreau-Yasuda model, s
d_r	diameter of RBC, m

DOI: 10.1002/fld

Subscript

k	plasma or RBC phases
n	total number of phases
r	RBC phases
p	plasma phase

Abbreviation

RBC	red blood cell
WBC	white blood cell
WSS	wall shear stress

ACKNOWLEDGEMENTS

This research was partially supported by the Wayne State University Institute for Manufacturing Research (IMR) under the grant 3-36037 and by the Wayne State University Office of the Vice President for Research under the grant 1-76068.

REFERENCES

1. Papaharilaou Y, Ekaterinaris JA, Manousaki E, Katsamouris AN. Stress analysis in abdominal aortic aneurysms applying flow induced wall pressure. *Fifth GRACM International Congress on Computational Mechanics*, Limassol, 29 June–1 July 2005.
2. Feldman CL, Stone PH. Intravascular hemodynamic factors responsible for progression of coronary atherosclerosis and development of vulnerable plaque. *Current Opinion in Cardiology* 2000; **15**(6):430–440.
3. Tiwari P. Multifield computational fluid dynamics model of particulate flow in curved circular tubes. *Theoretical and Computational Fluid Dynamics* 2004; **18**:205–220.
4. Dwyer HA, Cheer AY, Rutaganira T, Shacheraghi N. Calculation of unsteady flows in curved pipes. *Journal of Fluids Engineering* 2001; **123**:869–877.
5. Peattie RA, Riehle TJ, Bluth EI. Pulsatile flow in fusiform models of abdominal aortic aneurysms: flow fields, velocity patterns and flow-induced wall stresses. *Journal of Biomedical Engineering* 2004; **126**:438–446.
6. Wahle A, Mitchell SC, Ramaswamy SD, Chandran KB, Sonka M. Four-dimensional coronary morphology and computational hemodynamics. *Medical Imaging* 2001; **4322**:743–754.
7. Ku D. Blood flow in artery. *Annual Review of Fluid Mechanics* 1997; **29**:399–434.
8. Berger S, Jou L. Flows in stenotic vessels. *Annual Review of Fluid Mechanics* 2000; **32**:347–382.
9. Pedley TJ. *The Fluid Mechanics of Large Blood Vessels*. Cambridge University Press: Cambridge, 1980.
10. Cho YI, Kensey KR. Effects of the non-Newtonian viscosity of blood on flows in a diseased arterial vessel. Part I: steary flows. *Biorheology* 1991; **28**:241–262.
11. Box FM, van der Geest RJ, Rutten MC, Reiber JH. The influence of flow, vessel diameter, and non-Newtonian blood viscosity on the wall shear stress in a carotid bifurcation model for unsteady flow. *Investigative Radiology* 2005; **40**:277–294.
12. Fahraeus R, Lindqist T. The viscosity of the blood in narrow capillary tubes. *American Journal of Physiology* 1931; **96**(3):562–568.
13. Widmaier EP, Raff H, Strang KT. *Vander*, *Sherman*, *Luciano's Human Physiology*: *The Mechanisms of Body Function*. McGraw-Hill: New York, 2004.
14. Lightfoot EN. *Transport Phenomena and Living Systems*: *Biomedical Aspects of Momentum and Mass Transport*. Wiley: New York, 1974.
15. Tateshima S, Murayama Y, Villablanca JP, Morino T, Nomura K, Tanishita K, Vinuela F. In vitro measurement of fluid-induced wall shear stress in unruptured cerebral aneurysms Harboring Blebs. *Stroke* 2003; **34**:187–192.
16. Kerber CW, Imbesi SG, Knox K. Flow dynamics in a lethal anterior communicating artery aneurysm. *American Journal of Neuroradiology* 1999; **20**:2000–2003.

DOI: 10.1002/fld

17. Imbesi SG, Kerber CW. Analysis of slipstream flow in two unruptured intracranial cerebral aneurysms. *American Journal of Neuroradiology* 1999; **20**:1703–1705.
18. Johnston BM, Johnston PR, Corney S, Kilpatirick D. Non-Newtonian blood flow in human right coronary arteries: steady state simulations. *Journal of Biomechanics* 2004; **37**:709–720.
19. Johnston BM, Johnston PR, Corney S, Kilpatirick D. Non-Newtonian blood flow in human right coronary arteries: transient simulations. *Journal of Biomechanics* 2006; **39**:1116–1128.
20. Jung J, Lyczkowski RW, Panchal CB, Hassanein A. Multiphase hemodynamic simulation on pulsatile flow in a coronary artery. *Journal of Biomechanics* 2006; **39**:2064–2073.
21. Caro CG, Fitz-Gerald JM, Schroter RC. Arterial wall shear and distribution of early atheroma in man. *Nature* 1969; **233**:1159–1161.
22. Ohta M, Wetzel SG, Dantan P, Bachelet C, Lovblad KO, Yilmaz H, Flaud P, Rüfenacht DA. Rheological changes after stenting of a cerebral aneurysm: a finite element modeling approach. *CardioVascular and Interventional Radiology* 2005; **28**:768–772.
23. Gruttola SD, Boomsma K, Poulikakos D, Ventikos Y. Computational simulation of a non-Newtonian model of the blood separation process. *Artificial Organs* 2005; **29**:949–959.
24. Santamarina A, Weydahl E, Siegel Jr JM, Moore Jr JE. Computational analysis of flow I a curved tube model of the coronary arteries: effect of time-varying curvature. *Annals of Biomedical Engineering* 1998; **26**:944–954.
25. Komai Y, Tanishita K. Fully developed intermittent flow in a curved tube. *Journal of Fluid Mechanics* 1997; **347**:263–287.
26. Van Meerveld J, Waters SL. Numerical computation of the steady secondary flow in a tube with time-dependent curvature. *Journal of Mechanics and Applied Mathematics* 2001; **54**:631–640.
27. Buchanan JR, Kleinstreuer C, Comer JK. Rheological effects on pulsatile hemodynamics in a stenosed tube. *Computers and Fluids* 2001; **29**:695–724.
28. Gonzalez HA, Moraga NO. On predicting unsteady non-Newtonian blood flow. *Applied Mathematics and Computation* 2005; **170**:909–923.
29. Gidaspow D. *Multiphase Flow and Fluidization*: *Continuum and Kinetic Theory Descriptions*. Academic Press: New York, 1994.
30. Gijsen FJH, Allanic E, van de Vosse FN, Janssen JD. The influence of the non-Newtonian properties of blood on the flow in large arteries: unsteady flow in a 90 curved tube. *Journal of Biomechanics* 1999; **32**:705–713.
31. Wonjnaowski J. Numerical study of bileaf heart valves performance. *International Scientific Practical Conference*: *Efficiency of Engineering Education in XX Century*, Donetsk, Ukraine, May 2001; 29–31.
32. Eckmann DM, Bowers S, Stecker M, Cheung AT. Hematocrit, volume expander, temperature, and shear rate effects on blood viscosity. *Anesthesia and Analgesia* 2000; **91**:539–545.
33. *FLUENT 6.2 User's Guide*. Fluent Inc., 2005.
34. *GAMBIT 2.3 User's Guide*. Fluent Inc., 2005.
35. Ding J, Lyczkowski RW, Sha WT. Modeling of concentrated liquid–solids flow in pipes displaying shear-thinning phenomena. *Chemical Engineering Communications* 1995; **138**:145–155.
36. Myers JG, Moore JA, Ojha M, Johnston KW, Ethier CR. Factors influencing blood flow patterns in the human right coronary artery. *Annals of Biomedical Engineering* 2001; **29**:109–120.
37. Perktold K, Hofer M, Rappitsch G, Loew M, Kuban BD, Friedman MH. Validated computation of physiologic flow in a realistic coronary artery branch. *Journal of Biomechanics* 1998; **31**:217–228.
38. Perktold K, Kenner TH. Flow and stress characteristics in rigid walled and compliant carotid artery bifurcation models. *Medical–Biological Engineering—Computing*, Graz, Austria, 1993; 1–20.
39. Ernst W, Leonid G, Ulrich K, Klaus A. In-vivo coronary flow profiling based on biplane angiograms: influence of geometric simplifications on the three-dimensional reconstruction and wall shear stress calculation. *Biomedical Engineering Online* 2006; **5**:39.
40. Rindt CCM, van Steenhoven AA, Janssen JD, Vosser G. Unsteady entrance flow in a 90 curved tube. *Journal of Fluid Mechanics* 1991; **226**:445–474.
41. Schmid-Schonbein H, Wells R, Goldstone J. Influence of deformability of human red cells upon blood viscosity. *Circulation Research* 1969; **25**:131–143.
42. Stary HC. *Atlas of Atherosclerosis*: *Progression and Regression*. Parthenon Publishing: New York, 1999.

DOI: 10.1002/fld